2018 年度　公益財団法人日本台湾交流協会　フェローシップ事業成果報告書
（自然科学分野）

Abnormally Large Postseismic Deformation Caused by Reactivated Mud Diapirism on the Accretionary Wedge: Constrained by the 2016 Meinong Earthquake

蔡佩京
国立成功大学地域学系
招聘期間（2018 年 6 月 28 日～8 月 11 日）

2019 年
公益財団法人日本台湾交流協会

Abnormally Large Postseismic Deformation Caused by Reactivated Mud Diapirism on the Accretionary Wedge: Constrained by the 2016 Meinong Earthquake

Pei-Ching Tsai [a], Ruey-Juin Rau [a], Kuo-En Ching [b]

[a] *Department of Earth Sciences, National Cheng Kung University, Tainan, Taiwan*

[b] *Department of Geomatics, National Cheng Kung University, Tainan, Taiwan*

Keyword: 2016 Meinong earthquake, aseismic slip, triggered, inelastic process, mud diapir

1. Introduction

The moment released by the postseismic deformation is usually smaller than the coseismic deformation in subduction zones [e.g., Perfettini et al. 2005; Lin et al., 2013]. However, it is also not a unique case which the accumulative postseismic displacement is larger than or equal to the coseismic displacement in subductions detected by the geodetic observations [e.g., Heki et al., 2003; Suito et al., 2011; Geirsson et al., 2015; Howell et al., 2017]. The transition region from creeping to seismogenic zones based on the studies of 2004 Parkfield earthquake [e.g., Freed, 2007; Barbot et al., 2009] or a weakly coupled interface are usually proposed to generate abnormally large ratio of postseismic and coseismic displacements [Geirsson et al., 2015]. Nevertheless, those mechanisms are derived from the inverse of inland geodetic observations based on the assumption of the moment accumulation and release being on the interface [e.g., Heki et al., 2003; Suito et al., 2011; Geirsson et al., 2015; Howell et al., 2017]. In addition, if the coseismic slip occurs on the shallow part of interface with the constraint of inland measurements, while the postseismic slip is further downdip, the postseismic slip may cause relatively greater measured surface displacements compared to its moment released [Geirsson et al., 2015]. The reason to result in the abnormally large postseismic deformation is therefore still unclear. Moreover, the seismic hazard assessments are based on the seismic moment budget, so it is important to elucidate the factors to cause larger postseismic displacement in the subduction zone.

The 2016 M_w 6.4 Meinong earthquake in SW Taiwan (Figure 1) occurred on a gentle dip angle blind thrust with left-lateral motion [Huang et al., 2016]. An abnormal uplifting has been detected by the continuous GPS observations and DInSAR results during the coseismic period [Huang et al., 2016], which corresponds to the low S-wave pattern speeds at 0 - 4 km depths [Kuo-Chen et al., 2017]. The abnormal uplifting has been therefore proposed as the inelastic deformation of overpressure sediments triggered by the coseismic stress [Huang et al., 2016]. The SW Taiwan locates at the transition from subduction to collision [Rau et al., 2012] because the Wadati-Benioff zone is still detected [e.g., Rau et al. 1995, Huang et al., 2014] and the Manila trench connects the inland deformation in SW Taiwan [Liu et al., 1997] (Figure 1). The postseismic deformation associated with the 2016 Meinong earthquake consequently provides us a rare opportunity to understand the reason causing that the moment release by the postseismic deformation larger than one by coseismic deformation.

In this study, we used the 98 continuous GPS stations between 2012 and 2018 to characterize the coseismic and postseismic displacements of the 2016 Meinong earthquake. The coseismic source model is then estimated by the dislocation model [Okada, 1985, 1992]. To examine the possible mechanism to cause the postseismic deformation of this event, the viscoelastic relaxation model [Freed and Bürgmann, 2004; Freed et al., 2006], kinematic fault model [Okada, 1985, 1992], and afterslip model [Marone et al., 1991; Freed et al., 2006] were all adopted. Then the geological information is integrated together to solve the reason of abnormally large postseismic deformation.

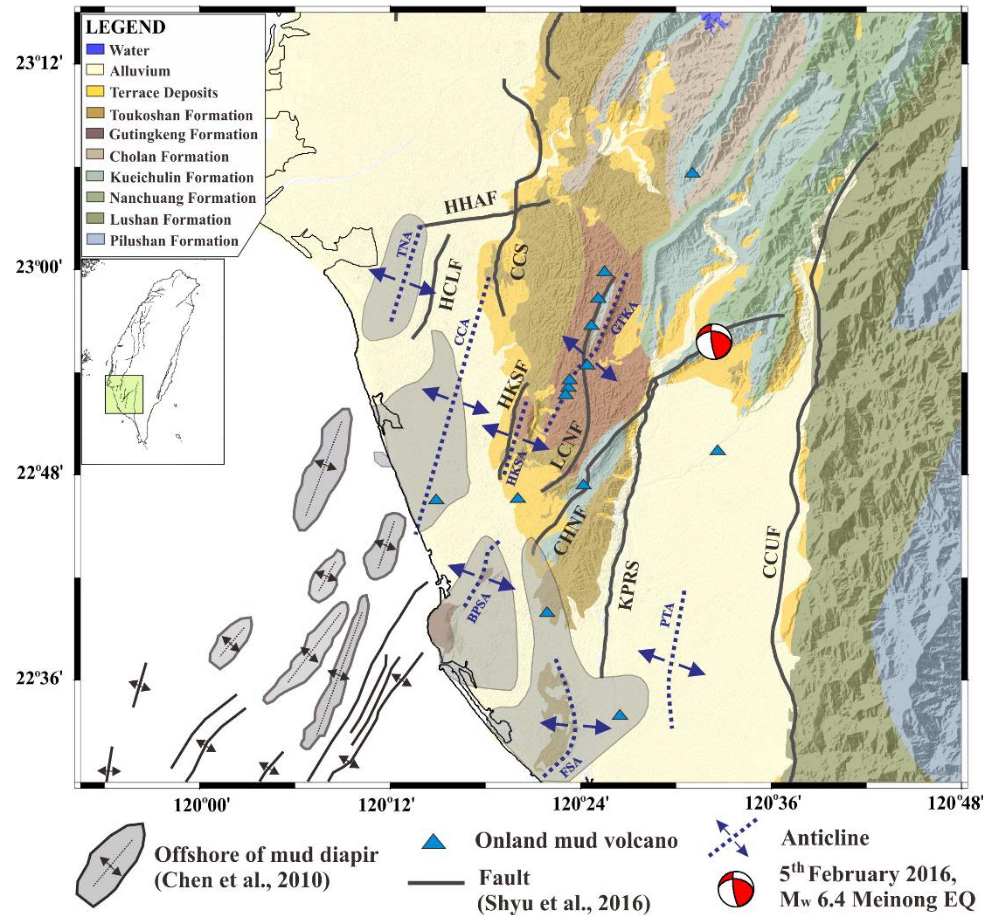

Figure 1. Geological map of SW Taiwan with the distribution of the mud diapir. Black lines show the faults, HHAF: Hsinhua fault; HCLF: Houchiali fault; CCS: Chungchou structure; HKSF: Hsiaokangshan fault; LCNF: Longchuan fault; CHNF: Chishan fault; KPRS: Kaopong river structure; CCUF: Chaochou fault. Blue dash lines show the anticline, TNA: Tainan anticline; CCA: Chungchou anticline; HKSA: Hsiaokangshan anticline; GTKA: Gutingkeng anticline; BPSA: Banpingshan anticline; FSA: Fongshan anticline; PTA: Pintung anticline.

2. Geological Settings

Southwestern Taiwan is the transitional zone from the subduction to the collision between the Philippine Sea plate and the passive continental margin of the Eurasian plate (Lacombe et al., 2001). The Pliocene to the Pleistocene foreland basin deposited the overpressure sediments by the rapidly mountain building and the flexure of the lithosphere due to the tectonic loading of the migrating orogenic in the SW Taiwan, the 5 km-thick mudstone was deposited, Gutingkeng formation. (Lin and Watts, 2002). Regionally abnormal uplifting during the coseismic period of Meinong earthquake was observed by the continuous GPS data adjacent the Gutingkeng anticline (Huang et al., 2016). The low permeable rock overlaid within the Gutingkeng formation, which is with the high fluid pressure. This overpressure sediments was disturbed by the coseismic stress, this inelastic deformation triggered the shallower thrust fault active to result the higher uplifting of the Lungchuan area. The NNE-SSW onland antiform structures were distributed in SW Taiwan (Figure 1.), parallel to the strike of the dominated faults and fold structures in Taiwan (Lacombe et al., 1999) and show the high correlation of the offshore mud diapir. These antiform structures were propagated by the thrust fold or the active of mud diapir due to the overpressure sediments covered by the low permeable material. The rapid uplifting rate of SW Taiwan cannot be predict well by dislocation model, Ching et al. (2015) proposed that besides the plate convergence force, the active of mud diapir is an additional source. The inelastic process contributed the surface deformation of SW Taiwan.

3. Coseismic and Postseismic Displacement Fields

3.1. Geodetic Data and Data Processing

In this study, we used the 98 continuous GPS stations which recorded the coseismic and postseismic displacement of the 2016 Meinong earthquake. These continuous GPS data were processed by GAMIT/GLOBK software v.10.4 (Tsai et al., 2017) to obtain the daily station coordinates solution in the reference frame of ITRF2008. In order to estimate the coseismic and postseismic displacements better, we remove the effects of interseismic velocity and seasonal variations by using the calibration function (Nikolaidis, 2002) to analyze the GPS time series.

$$\mathrm{y}(t_i) = \mathrm{a} + \mathrm{b}t_i + \mathrm{csin}(2\pi t_i) + \mathrm{dcos}(2\pi t_i) + esin(4\pi t_i) + fcos(4\pi t_i)$$
$$+ \sum_{j=1}^{n_g} gH(t_i - T_{gj}) + \sum_{j=1}^{n_h} h_j H(t_i - T_{gj})_{ti}$$
$$+ \sum_{j=1}^{n_k} k \exp\left[-(t_i - T_{kj})/\tau_j\right] H(t_i - T) + V_i \qquad (Eq.1)$$

where a is the intercept of the interseismic velocity, b is the interseismic velocity, c, d, e and f represent a year period and half year period variations, g is the coseismic displacement, h is the change rate of the velocity after the earthquake and k is the exponential decay of the postseismc displacement.

For estimating the precise coseismic and 419th postseismic displacements, we remove the interseismic velocity and the seasonal variations to emphasize the effect caused by the Meinong earthquake.

3.2. Coseismic and Postseismic Displacements

The coseismic displacements of the 2016 Meinong earthquake, from N to S, show counterclockwise rotation from NW to SW directions to the west of the epicenter with a maximum horizontal displacement of 39.2 mm. The coseismic vertical displacements indicate 5–35 mm uplifting west of the epicenter, with the highest value of 91 mm on the mud diaper anticline located 12 km W of the epicenter. The 13 months accumulated postseismic displacements reveal about 27.2 mm westward horizontal displacement and 5-39 mm vertical uplift displacements in the area south of the Hsinhua fault and north of the Chishan fault (Figure 2).

a. b.

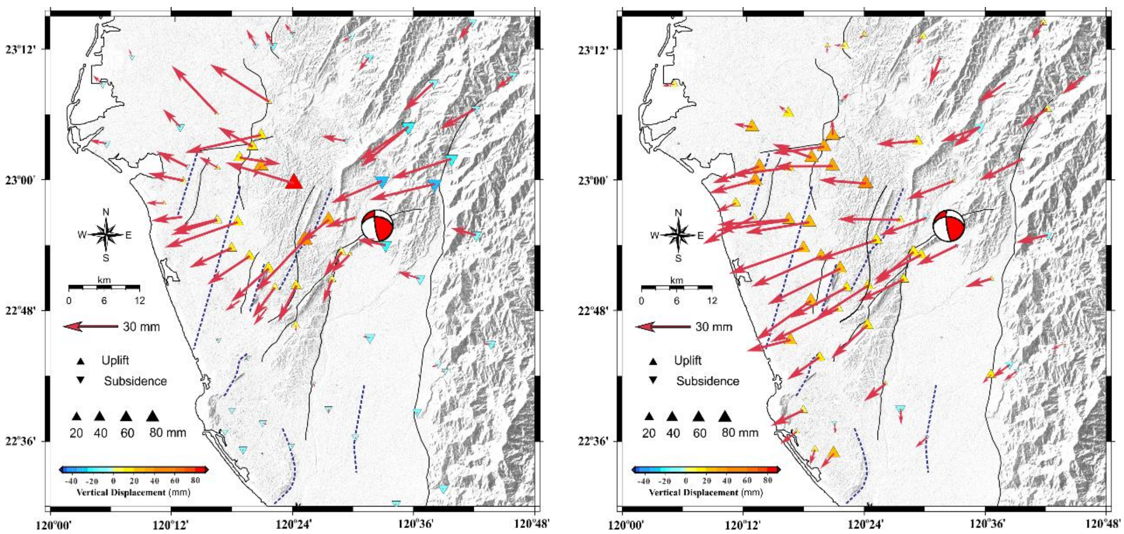

Fig 2. Coseismic and postseismic displacement of the 2016 Meinong earthquake. (a). The coseismic displacement of 2016 Meinong earthquake. (b). The postseismic displacement of 2016 Meinong earthquake. Focal mechanism denoted the Meinong earthquake. The pink arrows show the horizontal displacements. Triangle are symbolized the uplifted vertical displacement, and the inverted triangle are the subsided vertical displacement.

4. Source Models for Coseismic and Postseismic Deformations

4.1. Kinematic Coseismic Source Model

The fault ruptured during the Meinong earthquake does not extend to the surface. The fault geometries we used in this model are based on the mainshock focal mechanisms from the CWB (Central Weather Bureau) to search the optimal geometries for geodetic data. The conception of coseismic dislocation model is based on the formula: $\mathrm{d} = \mathrm{G(m)} \times \mathrm{s}$, which d is the observation displacement, s is the slip on the fault plane, G(m) is the Green's function in an elastic half-space (Okada, 1985) and m is the fault geometries. The optimum fault geometry for the coseismic dislocation model (Figure 3) indicates the strike of 293°, dip of 21° and the depth of 25 km, the main slip showed left-lateral with minor thrust motion in a depth range of 15-20 km and the maximum slip of 527 mm. The calculated coseismic geodetic moment is 5.00 $\times$ 10^{25} N-m and equivalent to M_w 6.43.

(a) (b)

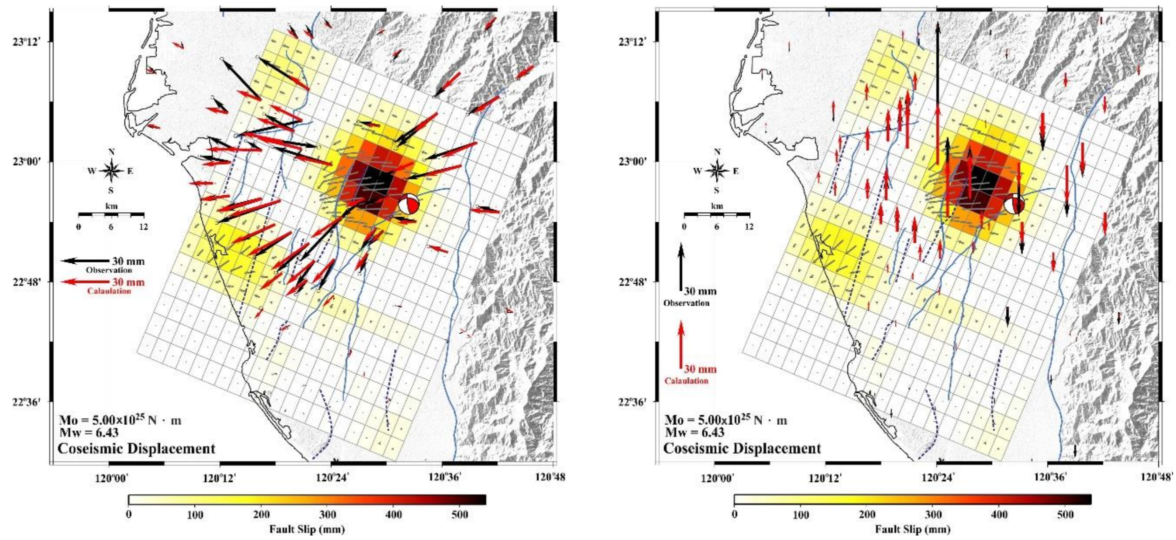

Fig 3: (a) The coseismic model result of the 2016 Meinong earthquake with the horizontal displacement. (b) The coseismic model result with the vertical displacement. Black arrows denoted the observed coseismic displacement. Red arrows denoted the calculated coseismic displacement which forward by the model. Gray arrows are the slip in the fault plane. Focal mechanism is the Meinong earthquake. Blue lines are the fault distribution.

4.2. Kinematic Postseismic Source Model

We use the same fault geometry with the coseismic model for the inversion of the postseismic slip in the 329 days (Figure 4). There are two main slip in the postseismic model, one is on the west of the coseismic main slip with the left-lateral and thrust motion, another one is on the shallow depth of 7-10 km with the thrust motion. The calculated postseismic geodetic moment is 7.90×10^{25} N-m and equivalent to M_w 6.57.

(a) (b)

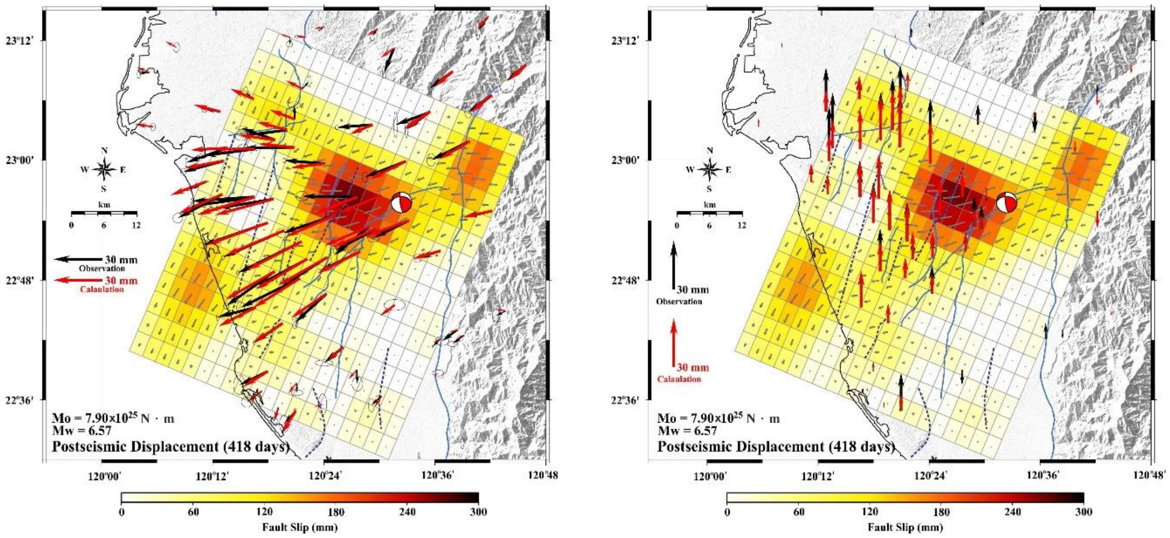

Fig. 4: (a) The postseismic model result of the 2016 Meinong earthquake with the horizontal displacement. (b) The postseismic model result of the 2016 Meinong earthquake with the vertical displacement. Black arrows denoted the observed coseismic displacement. Red arrows denoted the calculated coseismic displacement which forward by the model. Gray arrows are the slip in the fault plane. Focal mechanism is the Meinong earthquake.

4.3. Afterslip Model

Afterslip is the one of the primary mechanisms of the postseismic deformation following the mainshock (Marone et al., 1991). It was resulted by the coseismic stress change caused the aseismic creeping occurred surrounding the area of the asperity following the earthquake. In this model, we assumed that all of the postseismic deformation is induced by the afterslip. The model result showed that the direction of the calculation displacement is identical to the observation displacement, but the moment magnitude contributed by the afterslip is smaller than the observation which modeled by the postseismic dislocation model (Figure 5).

(a) (b)

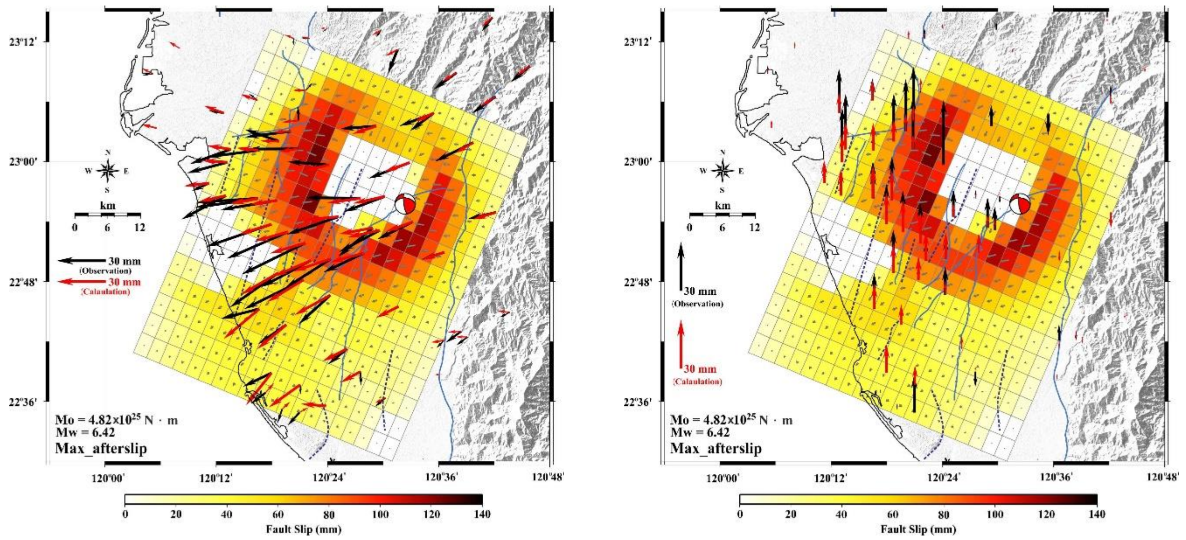

Fig. 5: (a) The result of the maximum_afterslip model with the horizontal displacement. (b) The result of the maximum_afterslip model with the vertical displacement. Black arrows denoted the observed coseismic displacement. Red arrows denoted the calculated coseismic displacement which forward by the model. Gray arrows are the slip in the fault plane. Focal mechanism is the Meinong earthquake.

4.4、Residual Model

The moment magnitude contributed by the afterslip is smaller than the observation which modeled by the postseismic dislocation model. Thus, we inversed the model by using the calculated displacement from afterslip model to minus the observation postseismic displacement, which called residual model. The result shown as Figure 6, we can figure out where is the source of extra energy to contribute the larger postseismic deformation following the 2016 Meinong earthquake. This extra energy distributions were overlap the mud diapirs (Figure 1).

(a) (b)

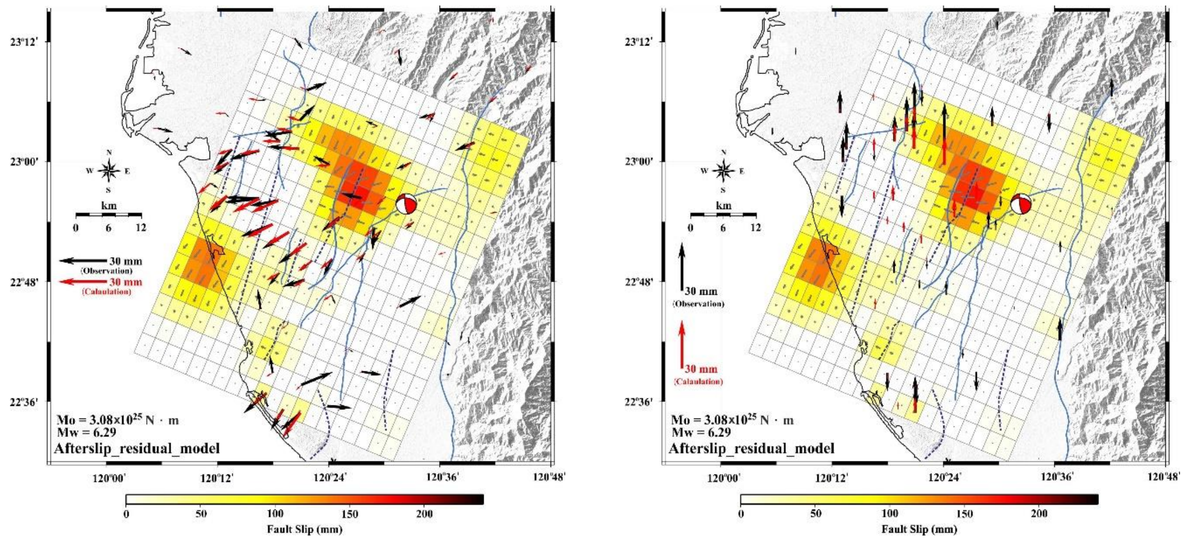

Fig. 6: (a) The result of the residual model with the horizontal displacement. (b) The result of the residual model with the vertical displacement. Black arrows denoted the observed coseismic displacement. Red arrows denoted the calculated coseismic displacement which forward by the model. Gray arrows are the slip in the fault plane. Focal mechanism is the Meinong earthquake.

5. Discussion

Coseismic and Postseismic moment release curve inferred for the 2016 Meinong Earthquake is showed at Figure 7. We estimated that the postseismic moment (Mw = 6.60) released greater than coseismic moment (Mw = 6.43) during the 720 days. The total magnitude released by Meinong earthquake is Mw 6.70.

The main mechanism of the postseismic deformation triggered by 2016 Meinong earthquake is the afterslip, but the moment magnitude of the afterslip couldn't contribute the enough energy for this postseismc deformation processing. Therefore, we presumed that the 5-km-thick mudstone of the Gutingkeng Formation coverage this area was activated by Meinong earthquake, this activation provide the remand energy for the postseismic deformation.

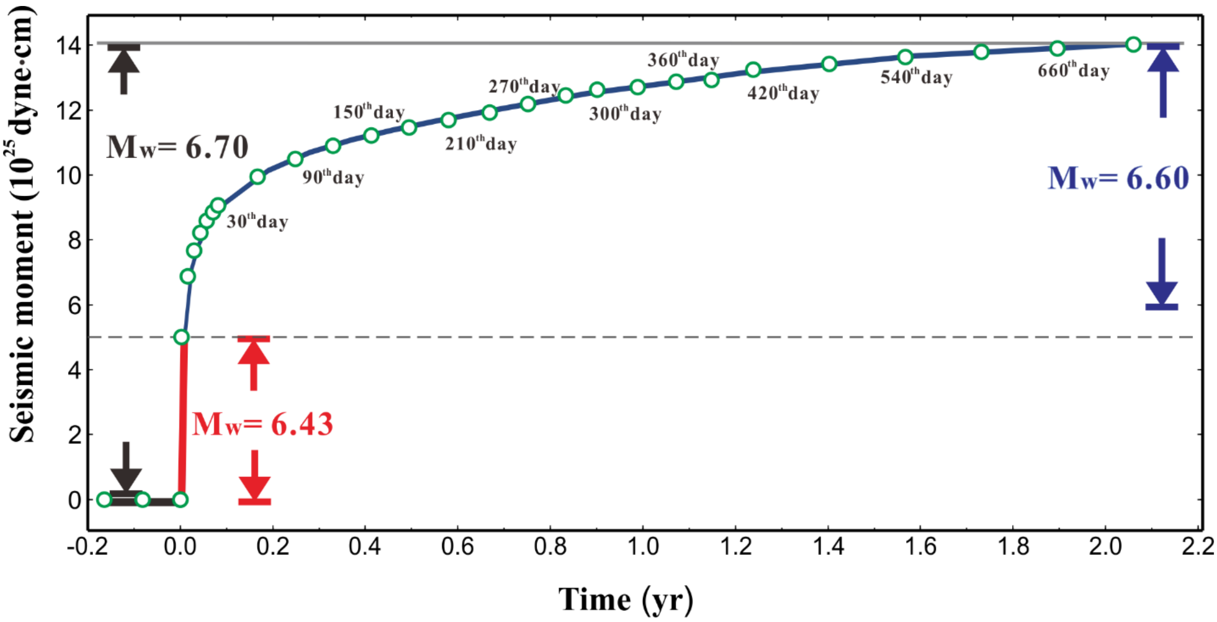

Fig. 7: Coseismic and Postseismic moment release curve inferred for the 2016 Meinong Earthquake. The red part denoted the moment release by the coseismic moment. The blue part is the moment released by the postseismic period. The black part is the total moment released by the 2016 Meinong earthquake.

For analyzing the variations of the deformation patterns to obtain the signal of the inelastic process for SW Taiwan, we separating the strain rate into long- and short- wavelength patterns to distinguish the deformation type before and after the earthquake events (Meneses-Gutierrez and Sagiya, 2016). The conception of this method is assumed that the surface observation are include the elastic and inelastic deformation. By using the moving average filtering to separate the strain rate into long- and short- wavelength patterns, long wavelength pattern denoted the elastic deformation which is the process of earthquake cycle, the cumulated and released of the earthquake energy, short wavelength were shown the inelastic deformation, which did not disturb by the earthquake. Thus, in this research we chose the 2003 Chengkung earthquake to be the source earthquake which is the far earthquake for SW Taiwan to banish from the effect of the earthquake (Figure 8 – Figure 10). Along the north of Chishan fault, there are the persistent compress signal which present the inelastic signal.

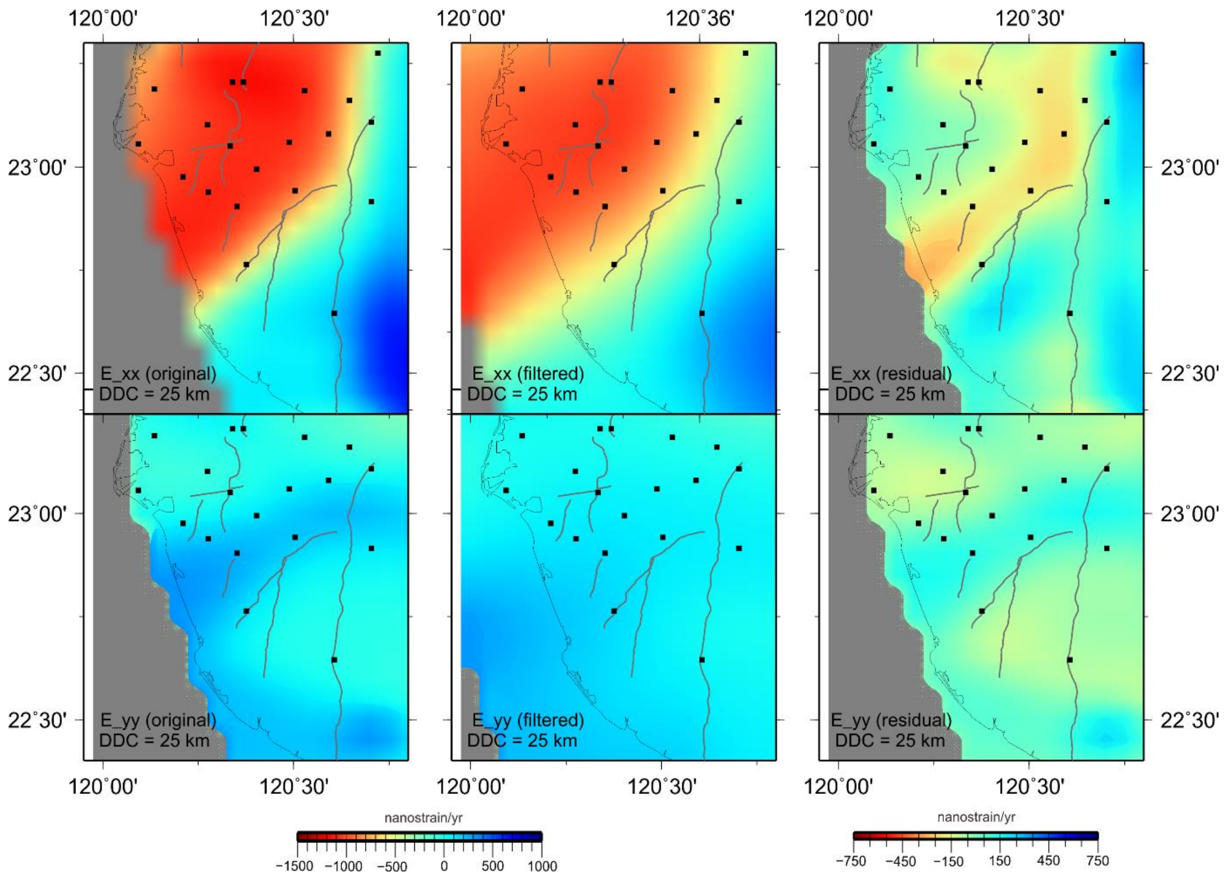

Fig. 8: Strain rate analysis from 2004 to 2005. Left figures are the observation; middle figures are the long-wavelength components retrieve from the moving average filter; right figures are the residual from observation minus the long-wavelength components, defined to be the short-wavelength components. Upper figures are the E-W strain rate in a circle with a radius of 20 km; bottom figures are the N-S strain rate in a circle with a radius of 20 km.

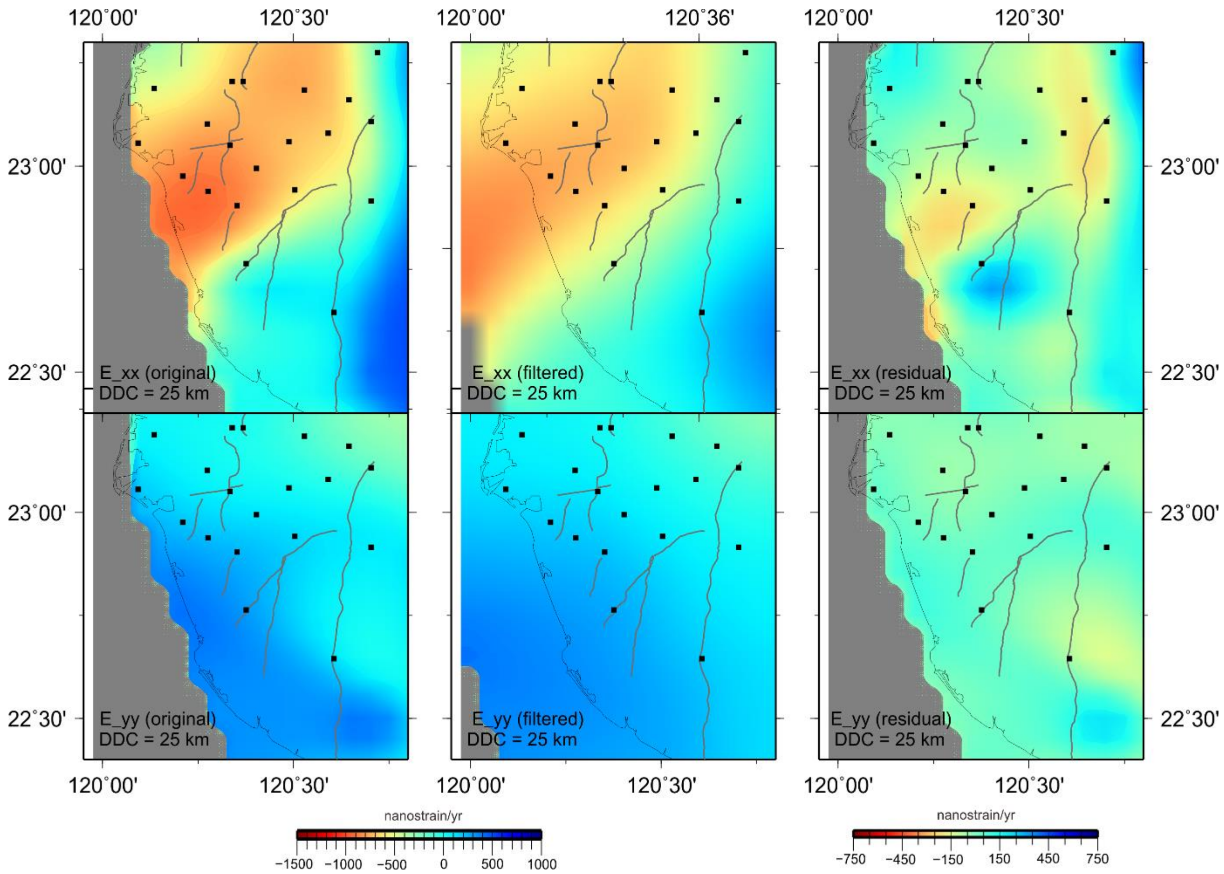

Fig. 9: Strain rate analysis from 2005 to 2006. Left figures are the observation; middle figures are the long-wavelength components retrieve from the moving average filter; right figures are the residual from observation minus the long-wavelength components, defined to be the short-wavelength components. Upper figures are the E-W strain rate in a circle with a radius of 20 km; bottom figures are the N-S strain rate in a circle with a radius of 20 km.

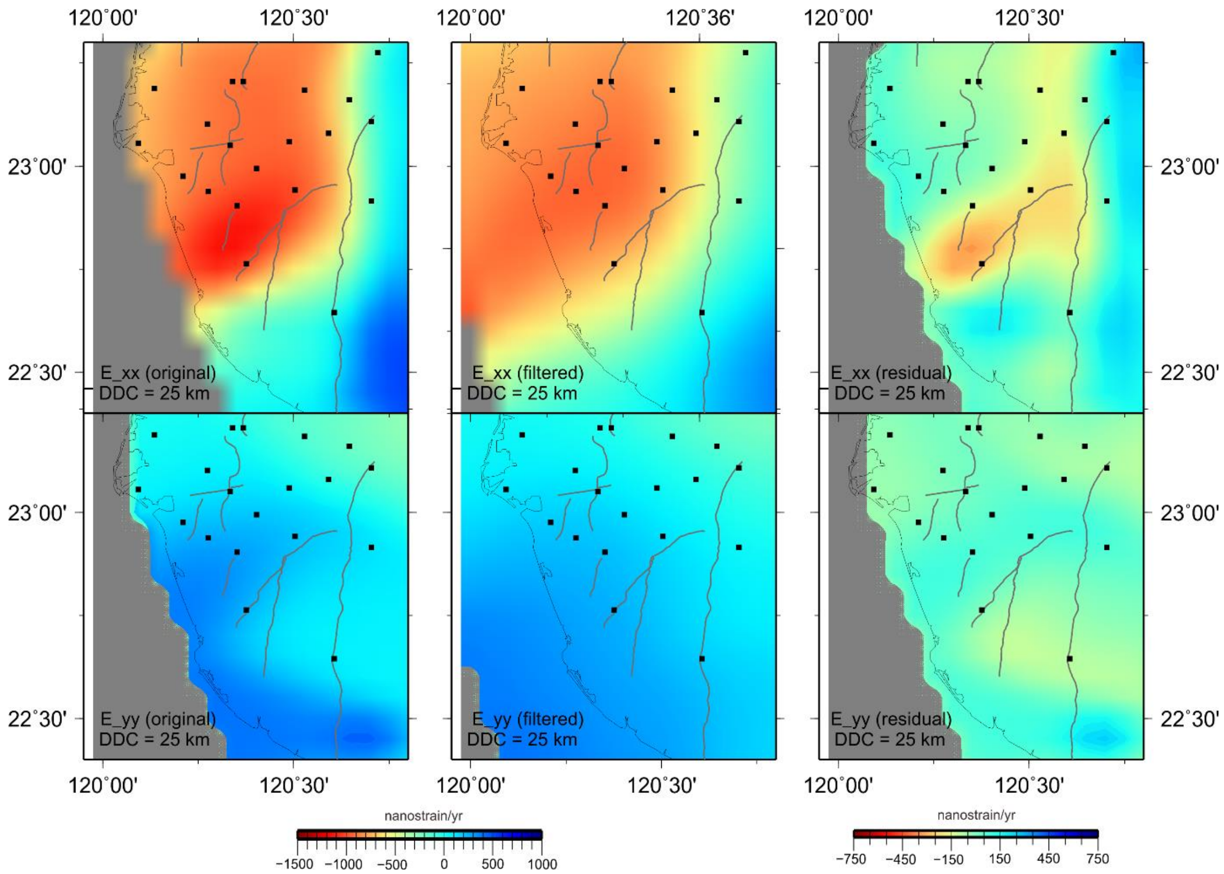

Fig. 10: Strain rate analysis from 2006 to 2007. Left figures are the observation; middle figures are the long-wavelength components retrieve from the moving average filter; right figures are the residual from observation minus the long-wavelength components, defined to be the short-wavelength components. Upper figures are the E-W strain rate in a circle with a radius of 20 km; bottom figures are the N-S strain rate in a circle with a radius of 20 km.

6. Conclusion

Postseismic deformation following the Meinong earthquake may require activations of the mud diapir on the accretionary wedge as the additional sources. We presumed that the coseismic stress triggered the inelastic process at the shallow sediments with thick mudstone, then the mud diapir active.

References

Chen, S.C., Hsu, S.K., Tsai, C.H., Ku, C.Y., Yeh, Y.C., and Wang, Y. (2010), Gas seepage, pockmarks and mud volcanoes in the near shore of SW Taiwan. *Marine Geophysical Researches*, 31, 133-147.

Ching, K.E., Gourley, J.R., Lee, Y.H., Hsu, S.C., Chen, K.H., and Chen, C.L. (2015), Rapid deformation rates due to development of diapiric anticline in southwestern Taiwan from geodetic observations. *Tectonophysics*, 692 (B), 241-251. doi.org:10.1016/j.tecto.2015.07.020.

Freed, A.M., and Bürgmann R. (2004), Evidence of power-law flow in the Majave desert mantle. *Nature*, 430, 548-551. doi:10.1038/nature02784.

Freed, A.M., Bürgmann R., Calais, E., Freymueller, J., and Hreinsdóttir, S. (2006), Implications of deformation following the 2002 Denali, Alaska, earthquake for postseismic relaxation processes and lithospheric rheology. *Journal of Geophysical Research,* 111 (B01401). doi:10.1029/2005JB003894.

Geirsson, H., Lafemina, P.C., DeMets, C., Hernandez, D.A., Mattioli, G.S., Rogers, R., Rodriguez, M., Marroquin, G., and Tenorio, V. (2015), The 2012 August 27 M_w 7.3 El Savador earthquake: expression of weak coupling on the Middle America subduction zone. *Geophys. J. Int.,* 202, 1677-1689. doi:10.1093/gji/ggv244.

Heki, K., Miyazaki, S., and Tsuji, H. (1997), Silent fault slip following an interplate thrust earthquake at the Japan Trench. *Nature,* 386, 595-598.

Howell, A., Palamartchouk, K., Papanikolaou, X., Paradissis, D., Raptakis, C., Copley, A., England, P., and Jackson, J. (2017), The 2008 Methoni earthquake sequence: the relationship between the earthquake cycle on the subduction interface and coastal uplift in SW Greece. *Geophys. J. Int.,* 208, 1592-1610. doi:10.1093/gji/ggw462.

Huang, M.H., Tung, H., Fielding, E., Huang, H.H., Liang, C., Huang, C., and Hu, J.C. (2016), Multiple fault slip triggered above the 2016 M_w 6.4 MeiNong earthquake in Taiwan.

Geophysical Research Letters, 43 (14), 7459-7467. doi.org:10.1002/2016GL069351.

Lacombe, O., Mouthereau, F., Angelier, J., & Deffontaines, B. (2001), Structural, geodetic and seismological evidence for tectonic escape in SW Taiwan. *Tectonophysics,* 333, 323-345. doi.org:10.1016/S0040-1951(00)00281-X.

Lin, A.T., and Watts, A.B. (2002), Origin of the West Taiwan basin by orogenic loading and flexure of the rifted continental margin. *Journal of Geophysical Research,* 107 (B9), 2185. doi .org:10.1029/2001JB000669.

Marone, C.J., Scholtz C.H., and Bilham R. (1991), On the mechanics of earthquake afterslip. *Journal of Geophysical Research,* 111 (B01401), 8441-8452.

Menese-Gutierrez, A., and Sagiya, T. (2016), Persistent inelastic deformation in central Japan revealed by GPS observation before and after the Tohoku-oki earthquake. *Earth and Planetary Science Letters,* 450, 366-371. doi.org:10.1016/j.epsl.2016.06.055.

Meneses-Gutierrez, A. and Sagiya, T. (2016), Persistent inelastic deformation in central Japan revealed by GPS observation before and after the Tohoku-oki earthquake. *Earth and Planetary Science Letters*, 450, 366-371, doi: 10.1016/j.epsl.2016.06.055

Suppe, J. (1984), Kinematic of arc-continent collision, flipping of subduction, and back-arc spreading near Taiwan. *Mem. Geol. Soc. China*, 6, 21-33.